Smart Materials and Structures

PAPER

Design and numerical performance analysis of a microgravity accelerometer with quasi-zero stiffness

To cite this article: Yuxing Duan *et al* 2020 *Smart Mater. Struct.* **29** 075018

View the article online for updates and enhancements.

Recent citations

- Analytical Study and Thermal Compensation for Capacitive MEMS Accelerometer With Anti-Spring Structure
  Hongcai Zhang *et al*

This content was downloaded from IP address 202.198.37.133 on 11/04/2021 at 12:34

IOP Publishing Smart Materials and Structures
Smart Mater. Struct. **29** (2020) 075018 (11pp) https://doi.org/10.1088/1361-665X/ab8838

Design and numerical performance analysis of a microgravity accelerometer with quasi-zero stiffness

Yuxing Duan[1], Xueyong Wei[1,2], Hairong Wang[1], Minghui Zhao[1], Ziming Ren[1], Huiying Zhao[1] and Juan Ren[3]

[1] State Key Laboratory for Manufacturing Systems Engineering, Xi'an Jiaotong University, Xi'an 710049, People's Republic of China
[2] State Key Laboratory of Applied Optics, Changchun Institute of Optics, Fine Mechanics and Physics, Chinese Academy of Sciences, Changchun 130033, People's Republic of China
[3] School of Construction Machinery, Chang'an University, Xi'an 710064, People's Republic of China

E-mail: seanwei@xjtu.edu.cn and juan.ren@chd.edu.cn

Received 1 November 2019, revised 22 March 2020
Accepted for publication 9 April 2020
Published 2 June 2020

Abstract
We report a nonlinear electrothermal-loaded accelerometer for microgravity measurement, achieving quasi-zero stiffness nearby its static equilibrium position. The high mechanical sensitivity is attributed to the compression of the spring, in addition to the geometric parameters matched with quasi-zero stiffness characteristic. To make the spring compressed effectively, a V-shape electrothermal actuator was adopted in the design. The FEA results in multiphysics clearly show the different performance of the accelerometer when it is at applied voltage or not, verifying that the electrothermal-loaded mechanism has an effective influence on the sensitivity of accelerometer. At the applied voltage of 22.3 V, the natural frequency of the accelerometer decreases from 501.95 Hz to 8.24 Hz, while the other two higher mode frequencies remain above 500 Hz. In addition, this mechanism realizes a quasi-zero stiffness approximately of 0.007 N m^{-1} within a linear working range of ± 400 μg and the stiffness becomes larger beyond this range protecting the device being overloaded.

Keywords: microgravity accelerometer, electrothermal-actuator, MEMS, quasi-zero stiffness

(Some figures may appear in colour only in the online journal)

1. Introduction

The earth's gravity field contains an abundance of information and measuring the tiny variations of the local gravitational acceleration has greater significance nowadays, which can provide us the information about earth's internal activities of seismic signals and also is helpful for mineral detection [1]. In contrast to traditional microgravity measurement devices like LaCoste land gravimter and Scintrex CG serise, the advantages of light-weight and portability make minuaturized devices being suitable for distributed gravity monitoring or measurement arrays. Therefore, micromechanical gravity accelerometers based on micro-electromechanical-system (MEMS) technology have attracted wide attention owing to their merits of mass production, light-weight, and low-cost. Although it seems like the MEMS devices could never attain the sensitivity of absolute devices, or the stability of superconducting gravimeters, MEMS is a feasible technology to achieve measurement level of relative spring-based gravimeter like Scintrex CG 5 having a low resonat frequency of 3 Hz [2]. In 2008, Sandia National Laboratory designed an optical acceleration sensor that adopted folded spring structures to achieve a natural frequency at 36 Hz [3]. Wu proposed a capacitive accelerometer using several long folded springs to achieve a resonant frequency of 13 Hz [4]. A MEMS seismometer with a lower resonat frequency of 6 Hz was developed by researchers from Imperial College and landed on Mars by the NASA's InSight mission [5].Thus, in order to measure the tiny changes of gravity acceleration, a rather sensitive structure is essential for MEMS gravity accelerometers. The spring—mass system

 © 2020 IOP Publishing Ltd Printed in the UK

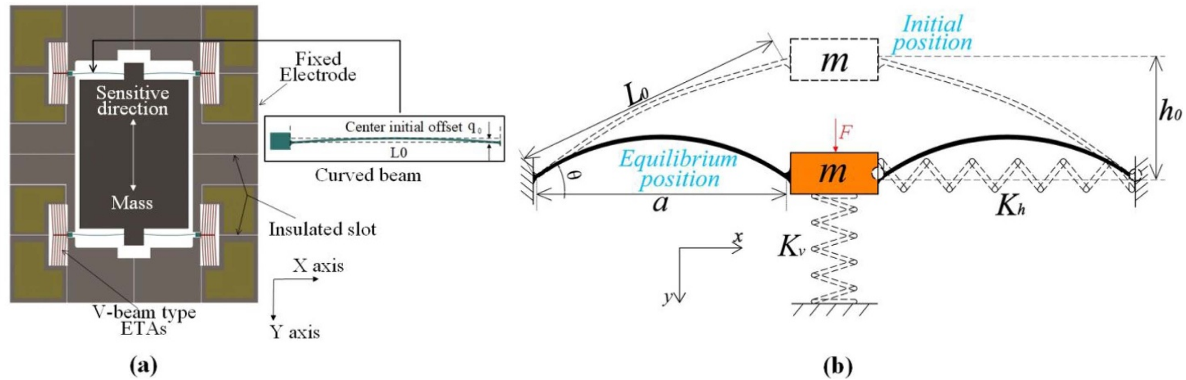

Figure 1. (a) Front view of accelerometer chip layout (inset figure shows the detailed structure of the curved beam). (b) The simplified mass-spring model of the microgravity accelerometer.

of MEMS devices can be divided into two different types: linear and nonlinear structures. For the former usually used in devices having the first order mode of out-of-plane vibration, the straight beam is widely used. S Kavitha has studied a low natural frequency MEMS accelerometer (103.8 Hz) for concrete SHM (Structural Health Monitoring) application, using four straight beams which are distributed horizontally and longitudinally and showing linear deflection versus acceleration [6]. A Quad beam structure that each of cantilevers shaped like the letter L was designed in J A Plaza's accelerometer, which has a simulated frequency of 489 Hz for first mode [7]. For the devices having the first order mode of in-plane vibration, there are usually two kinds of structures both linear and nonlinear. J T Teo used 7 μm wide straight cantilever as spring structure in MOEMS accelerometer, of which first resonant frequency is 2.33 kHz [8–10]. Folded beam is one of the most common configurations in linear springs. Other examples of folded beam which was developed by W Hortschitz, were used in many MEMS devices, such as vibration sensor, inclination sensor, electric field strength sensor and so on [11–16], and most of them have the natural frequency above 100 Hz. Nonlinear springs have been increasingly studied as well, e.g. a four sets of bilateral symmetric angled beams and curved beams are respectively used in the devices designed by D S Nguyen [17, 18], of which the resonant frequency is above 500 Hz. Combining curved beam and linear spring, B Vysotskyi designed devices [19–21] to form nonlinear characteristic of suspended structures and have a large bandwidth of 5 $\sim$ 100 Hz in a very low frequency domain. Similarly, parallel curved springs were used in MEMS devices [22–24] to improve its nonlinear mechanical characteristic. Some scholars have used electrostatic force effect as the mechanical spring to construct a nonlinear system [25, 26], where nonlinear behaviour in these devices was observed. Consequently, due to the fact that linear springs characteristic is limited by dimension limitation in MEMS manufacturing process, most MEMS are not sensitive enough to measure tiny variations in gravity acceleration effectively. For example, to measure a 40 μGal (1 Gal = 1 cm s^{-2}) peak g-value change of the earth's tides, a 2 Hz natural frequency for a displacement sensitivity of $\leqslant$2.5 nm $\left(\sqrt{\mathrm{Hz}}\right)^{-1}$ is required [27]. These nonlinear characteristic could help to significantly increase the sensitivity of devices than using linear structure in the same dimensions, although causing a drawback of a narrow response region.

In the low-frequency vibration isolation, there is also a similar issue that the natural frequency reduction of vibration isolation system is also limited by its stiffness and load capacity. Generally, an effective linear isolator is only at input frequency greater than $\sqrt{2}$ time the natural frequency [28]. Therefore, isolators with nonlinear characteristics have attracted a great deal of interests among scholars, who are engaged in low-frequency vibration isolation. One type of nonlinear isolator is based on geometric anti-springs, of which the modal frequency system can be decreased with the increase of the applied force. Based on this concept, scholars from Glasgow University have used large length-wide ratio and high aspect ratio flexure cantilevers in their proposed MEMS microgravity accelerometer [29] to realize this mechanism, which has challenged the limit of MEMS device fabrication technology, achieving an ultra-low resonance frequency of 2.3 Hz. Similar to this work, Mansouri developed a high resolution MEMS gravimeter using the buckling behaviour of spring structure [30]. Zhang utilized anti-spring structures in their capacitive accelerometer and its performance improvement was validated [31]. Other systems are using two parts of springs to realize quasi-zero stiffness characteristics [32–35], which are generally combined in parallel with a positive stiffness mechanism and a negative stiffness mechanism. Tang adopted bi-stable curved beams and folded beams in their MEMS gravimeter, achieving a low resonant frequency of 3.1 Hz [36]. The function of the negative stiffness structure is to compensate a portion of the positive stiffness, so that the system stiffness near the static equilibrium position could approach zero. The main advantage of quasi-zero stiffness is that there is no need for downsizing structure to acquire low-frequency as in the case of a linear system.

In this work, we adopt the concept of quasi-zero stiffness to design a microgravity accelerometer. The working principle of proposed microgravity accelerometer together with a modelling of the quasi-zero stiffness characteristics and electrothermal actuator are first analysed and discussed in section 2. Then, the modal simulation and static analysis based on FE

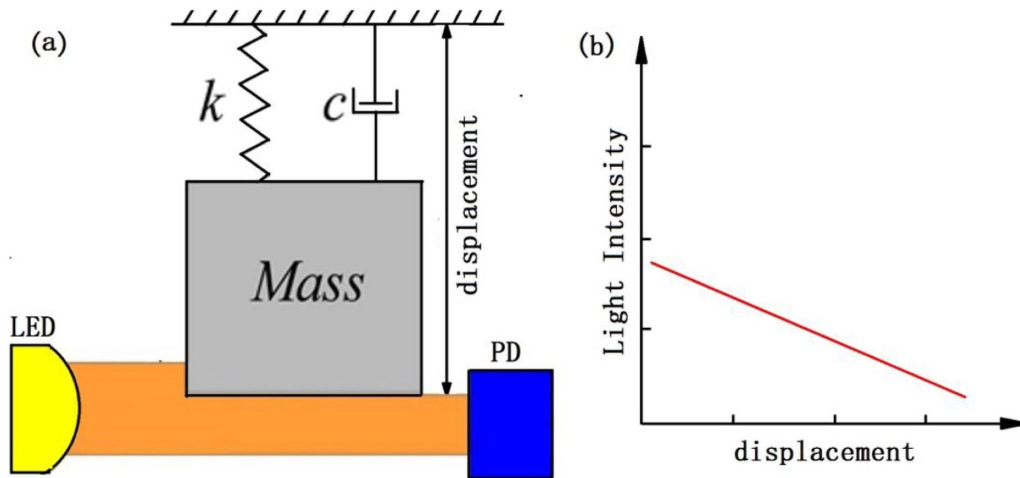

Figure 2. A schematic of the proposed displacement measurement principle.

analysis is discussed in section 3. Finally, the main conclusions are given in section 4.

2. Working principle

A schematic of the designed microgravity accelerometer is shown in figure 1(a) and it can be simplified as a spring-mass system as shown in figure 1(b). Under the variation of external gravity acceleration, the suspended mass on springs moves up and down, and the position of proof mass changes accordingly. In the low-frequency measurement when the excitation frequency ω is far less than the resonant frequency ω_0, the acceleration that the proof mass is subjected to is nearly proportional to its displacement as shown in the following equation:

$$a = \omega_0^2 \cdot x \quad (1)$$

Where, a is the acceleration experienced by proof mass and x is relative displacement. Therefore, the relative microgravity acceleration can be obtained by measuring the displacement of proof mass, and the higher displacement sensitivity, the higher accuracy of measured acceleration [37]. The measurement principle is schematically shown in figure 2, where the MEMS chip is placed between a light source (LED) and a photodiode (PD). The proof mass changes its position when it is subject to an acceleration and accordingly adjust the light into PD. Therefore, the output light intensity is changed linearly with the displacement. As a result, a larger displacement of mass is expected when a tiny acceleration changes if a higher resolution is necessary. Accordingly, a lower stiffness is required to obtain larger displacement for a given load, but a larger stiffness is needed to protect the device in case of overloading like a shock. For this reason, the proposed design is expected to have a nonlinear force-displacement relationship. In addition, micro electrothermal actuator is designed to control the state of each curved beam and accordingly the mechanical stiffness of the mass spring system can collectively controlled. This mechanism of changing sensitive stiffness

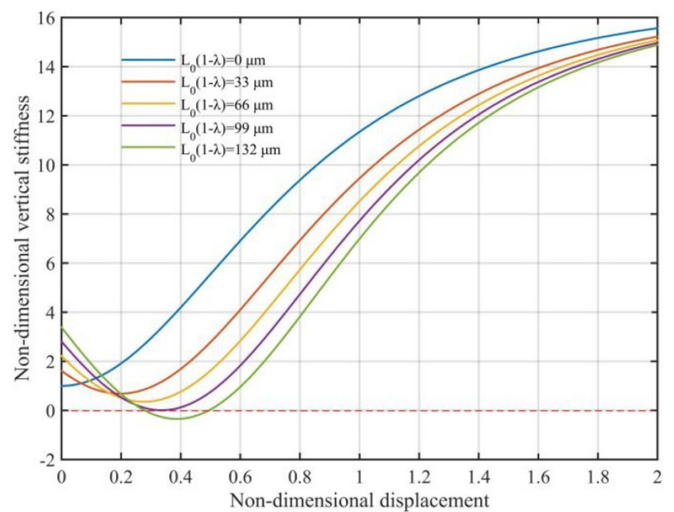

Figure 3. The curve of stiffness with different set of compression displacement and $\beta = 8$.

could be a novel method for low frequency measurement and adjustable working range. At the same time, the device is not necessarily designed with springs of larger length-width ratio or proof mass of larger dimensions, reducing fabrication difficulty efficiently. Like the systems which have high-static and low-dynamic stiffness [38], the proposed microgravity accelerometer can achieve quasi-zero stiffness characteristic on the condition that an original load capacity is set.

2.1. Accelerometer chip layout and spring structure design

SOI (Silicon on Insulator) was chosen as chip's material, which is a common material in MEMS devices. Figure 1(a) shows the layout (border size is 10 × 12 mm) of the designed accelerometer. The proof mass is at equilibrium position suspended by curved beam springs at the four corners. Each spring is equipped with a set of V-beam type thermal actuators, which can exert an axial force on the end of curved

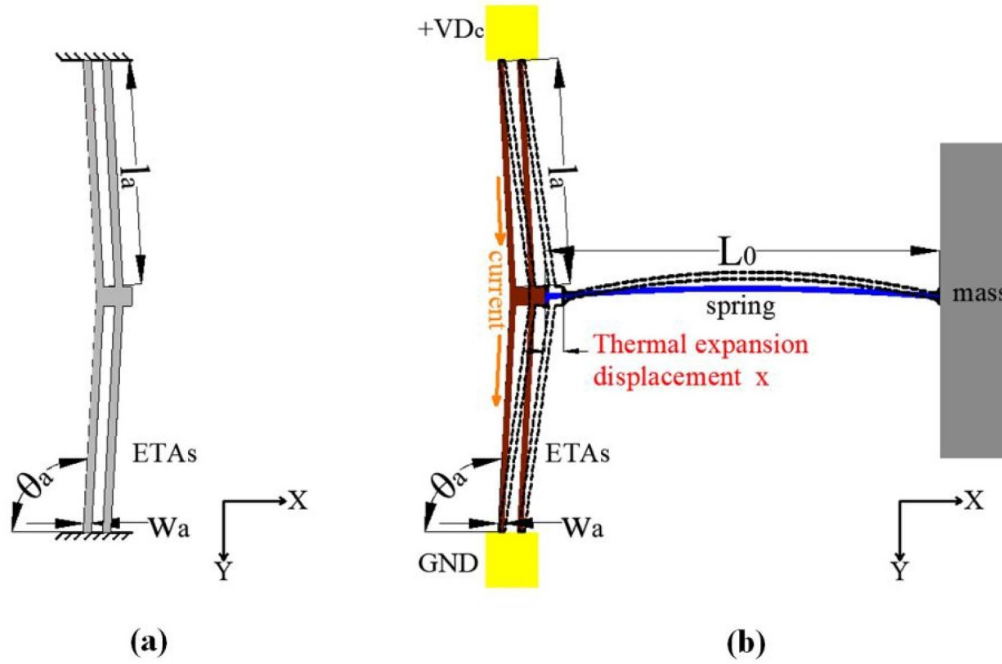

Figure 4. (a) The structure of an electrothermal V-shape actuator. (b) The diagram of loading mechanism with V-shape actuator.

beam spring when a proper voltage is applied at fixed electrode because of Joule heating and thermal expansion effects. There are several insulated slots between different electrodes and electrodes and frame to restrict the current only to passing through actuators.

As shown in figure 1, the spring is designed as a series of curved beams with a certain length-width ratio and a certain initial offset at beam's center, which looks like a part of large curvature arc. Owing to its shape, the spring would be buckling when the applied axial force is over the critical value. Because of symmetric axial forces to the mass, it is theoretically fixed at its original equilibrium position with four springs compressed simultanously.

2.2. Static characteristic of the sensitive unit

The microgravity accelerometer is simplified as a model of springs-mass system, in which the inward sides of two lateral curved beams are fixed to the mass and outward sides are fixed to the border as shown in figure 1(b). The central proof mass is only a few milligrams and the spring span is only a few millimeters. After the device is microfabrication and mounted as shown in figure 1(a), the initial position of proof mass may differ from its equilibrium position, where the line between two ends of spring end is horizontal. From the initial position to the equilibrium position, the springs change from original length to compressed state. In this model, the boundary of the spring end is a fixed anchor point, so it can be considered as clamped end. Thus, when the springs-mass is analyzed as a whole, it can be considered that the clamped end provides a certain y-axis (vertical) bearing capacity for the mass. Additionally, the curved beam itself has resistance to bending deformation along the x-axis, namely having axial stiffness. Therefore, the curved beam spring can be viewed as three linear springs, one fixed in vertical direction and one pair of springs hinged at both ends (in the small deflection, it can be approximately considered as linear springs). The static analysis of curved beam spring is given as follows.

First of all, the restoring force of the lateral springs can be expressed as:

$$F = 2K_h\left(L_0 - L\right)sin\theta \tag{2}$$

Where, K_h is the stiffness of the lateral spring, L_0 is the original length of the lateral spring and L is the length after compression. Noting that the lateral springs are at an angle θ from the horizontal and $sin\theta = \left(h_0 - y\right)/L$ in which h_0 is the vertical distance between the initial position and the equilibrium position, and y is the vertical displacement from the initial position as figure 1(b).

According to the Pythagorean theorem, $L_0 = \sqrt{{h_0}^2 + a^2}, L = \sqrt{\left(h_0 - y\right)^2 + a^2}$, so the equation (2) can be written as:

$$F = 2K_h\left(h_0 - y\right)\left(\frac{\sqrt{{h_0}^2 + a^2}}{\sqrt{\left(h_0 - y\right)^2 + a^2}} - 1\right) \tag{3}$$

After the dimensionless treatment, equation (3) can be rewritten as:

$$\frac{F}{K_h L_0} = 2\left(\sqrt{1-\lambda^2} - \tilde{y}\right) \times \left\{\left[\tilde{y}^2 - 2\sqrt{1-\lambda^2}\cdot\tilde{y} + 1\right]^{-1/2} - 1\right\} \tag{4}$$

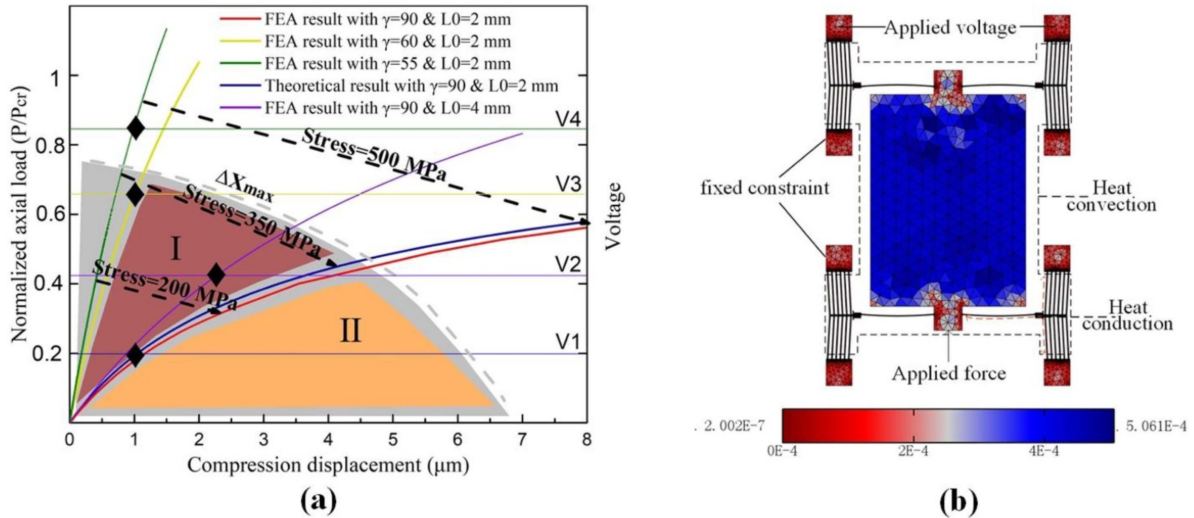

Figure 5. (a) Combinations of compression displacement and curved beam's stiffness that realize quasi-zero stiffness characteristic at various applied voltages (V1–V6 increases gradually). (b) Meshed FE model of the major structure of accelerometer in COMSOL.

Where, the dimensionless vertical displacement $\widetilde{y} = y/L_0$ and the geometrical parameter $\lambda = \frac{a}{L_0}$.

Then, taking into account the parallel vertical springs, the total force applied to the mass in the sensitive direction is the vertical component of the spring restoring force of lateral springs plus the vertical spring restoring force. On the basis of equation (4), the total force F of the system is normalized with $1/K_v L_0$:

$$\tilde{F} = \frac{F}{K_v L_0} = \tilde{y} + 2\beta\left(\sqrt{1-\lambda^2} - \tilde{y}\right) \times \left\{\left[\tilde{y}^2 - 2\sqrt{1-\lambda^2}\cdot\tilde{y} + 1\right]^{-1/2} - 1\right\} \quad (5)$$

Where, the stiffness of the vertical spring is defined as K_v and the stiffness ratio of the lateral springs to the vertical spring is defined as $\beta = K_h/K_v$.

After the differentiating equation (5), the expression of the dimensionless vertical stiffness of the mass-spring system is obtained:

$$\tilde{K} = 1 + 2\beta\left[1 - \frac{\lambda^2}{\left(\tilde{y}^2 - 2\sqrt{1-\lambda^2}\cdot\tilde{y} + 1\right)^{3/2}}\right] \quad (6)$$

It can be seen from figure 3 that for a given ratio value, as the axial compression displacement increases (the geometrical parameter λ decreases), the vertical stiffness of the system gradually decreases in a certain area, even below zero stiffness, showing a certain negative stiffness effect. In fact, re-derivation of equation (6) reveals that the lowest point of the drop occurs at the initial static equilibrium position $\tilde{y}_e = \sqrt{1-\lambda^2}$. It also can be seen from equation (6) that the value of $\tilde{K}$ is determined by β and λ. Therefore, when $\tilde{K} = 0$, the relationship between β and λ that satisfies the quasi-zero stiffness characteristic at the static equilibrium position $\tilde{y}_e$ is obtained:

Table 1. Different parameter values for the proposed accelerometer's structure that are used for modelling.

Parameters	Value
Spring span	2 mm
Spring width	22 μm
Spring center initial offset	40 μm
V-type beam length	1.2 mm
V-type beam width	30 μm
V-type beam initial angle	3°
Chip's device layer thickness	40 μm
Electrode material	Copper
Device layer material	Single crystal silicon
Electrical conductivity	260 S m^{-1}
Density	2330 kg m^{-3}
Thermal expansion coefficiency	2.6e–6 K^{-1}
Thermal conductivity	138 W (m · K)$^{-1}$
Convective heat transfer coefficient	400 W (m^2 · K)$^{-1}$
Room temperature	293 K

$$\lambda = 2\beta/(2\beta + 1) \quad (7)$$

Here, β is an independent variable. Similarly, taking λ as independent variable, the value of β is

$$\beta = \lambda/2(1-\lambda) \quad (8)$$

Equation (8) provides an important implication for designing this kind of quasi-zero stiffness system, which is obtained by the proper combination of the spring's compression displacement and the ratio of spring's axis stiffness K_h to its vertical stiffness K_v.

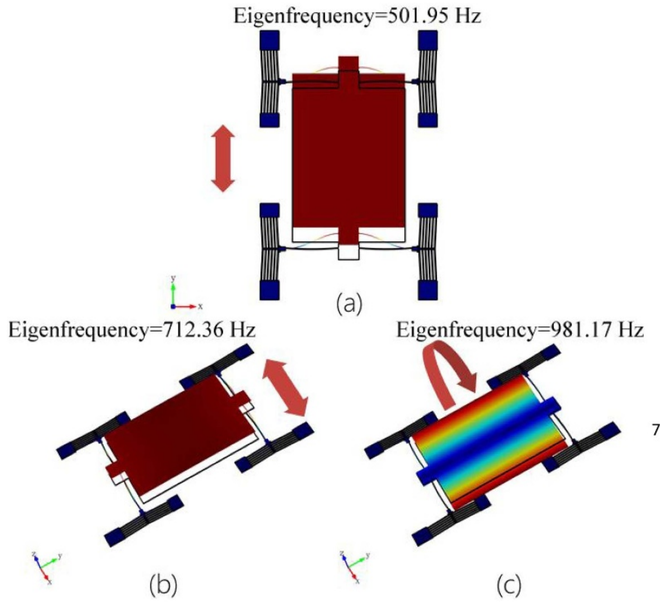

Figure 6. Eigenmodes of the designed accelerometer from COMSOL: (a) in-plane mode; (b) out-of-plane mode; (c) twisting mode.

2.3. Electrothermal actuator modelling

In order to achieve a certain amount of compression of the springs on both sides at the static equilibrium position in the aforementioned model, V-shape electrothermal actuators as shown in figure 4(a) are designed to generate compressing forces on the curved beam springs. The V-shape actuator can generate relevant heat when an electric current passes through the beam. The thermal expansion caused by the Joule heating makes the V shape actuator produce an axial force applied on the curved beam springs as shown in figure 4(b).

As the case in figure 4(b), it is assumed that the two ends of the V-shape actuator are anchored and actuator's centre only move along x-axis. The maximum apex displacement of a V-shape actuator could be expressed as follows [39]:

$$\Delta x_{max} = \frac{\alpha \cdot l_a \cdot \Delta T \cdot sin\theta_a}{\left(\frac{w_a}{l_a}\right)^2 + sin^2\theta_a} \tag{9}$$

Where, α is thermal expansion coefficient of the material, l_a, w_a, θ_a are the length, width and incline angle of a beam respectively. ΔT is the average temperature along the V-shape beam, which is mainly determined by the applied voltage and ambient temperature. Noting that the proof mass would be stable if the four actuators are driven at the same voltage. When the curved beam is connected to the actuator, the apex displacement of the V-shape actuator, namely the compression displacement subjected to loading of curved beam is expressed as follows:

$$x = \frac{\Delta x_{max}}{1 + \frac{K_h}{K_a}} \tag{10}$$

Where, K_a is the actuator's output stiffness and it can be expressed as:

$$K_a = \frac{4sin^2\theta_a w_a h_a E cos\theta_a}{l_a} \tag{11}$$

Where, h_a is the actuator's thickness and E is the actuator materials' Young's modulus.

After substituting equations (9) and (11) into equation (10), one can find that if the actuator's dimension are determined, its apex displacement is directly related to the applied voltage and the stiffness K_h. For the designed curved beam, its relation between the axial load P and end compression displacement x can be given by [40]:

$$P = P_{cr}\left\{1 - \pi\frac{q_0}{L_0}\left[\left(\pi\frac{q_0}{L_0}\right)^2 + 4\frac{x}{L_0}\right]^{-1/2}\right\} \cdot \left[1 + \frac{1}{8}\left(\pi\frac{q_0}{L_0}\right)^2 + \frac{1}{2}\frac{x}{L_0}\right] \tag{12}$$

where, $P_{cr} = \pi^2 EI/(0.5L_0)^2$ is the classical Euler critical load for fixed–fixed boundary. EI and q_0 are the flexural rigidity and the initial central offset of the curved beam respectively. Differentiating equation (12) with respect to x, one can get the axial stiffness of the curved beam.

$$K_h = P_{cr}\left\{\frac{\pi(q_0/L_0)\cdot\left[(\pi(q_0/L_0))^2 + x/L_0 + 2\right]}{L_0\left(4x/L_0 + (\pi(q_0/L_0))^2\right)^{3/2}} - \frac{\pi(q_0/L_0)/\left(\left(4x/L_0 + (\pi(q_0/L_0))^2\right)^{1/2}\right) - 1}{2L_0}\right\} \tag{13}$$

Therefore, considering that curved beam springs have various K_h, K_v with different dimensional parameters like the beam length-width ration $\gamma = L_0/w$ and beam length, we can infer a comprehensive interaction of different parameters which satisfy quasi-zero stiffness according to equations (8), 10 and (13). As shown in figure 5(a), some FEA curves were given in the case of $L_0 = 2$ mm and $q_0/L_0 = 0.02$. It can be seen that the K_h increases with the decreased γ. The similar trends would happen when L_0 increases and the γ remains the same. Specially, a theoretical result according to equation (12) was also calculated to show an accordance with FEA result. There are two boundary in figure 5(a), one is restricted by Δx_{max} line, which shows an inverse relation between the ETAs' maximum apex displacement and K_h at a determined actuator's dimension and applied voltage, the other is allowable stress line of silicon, which means out of the line a fracture happens. Taking relevant above-mentioned parameters into consideration, one can get some of crossover points (black rhombus) on different curves, which meet the requirements of quasi-zero stiffness. When γ increases, it is necessary to use much higher loading

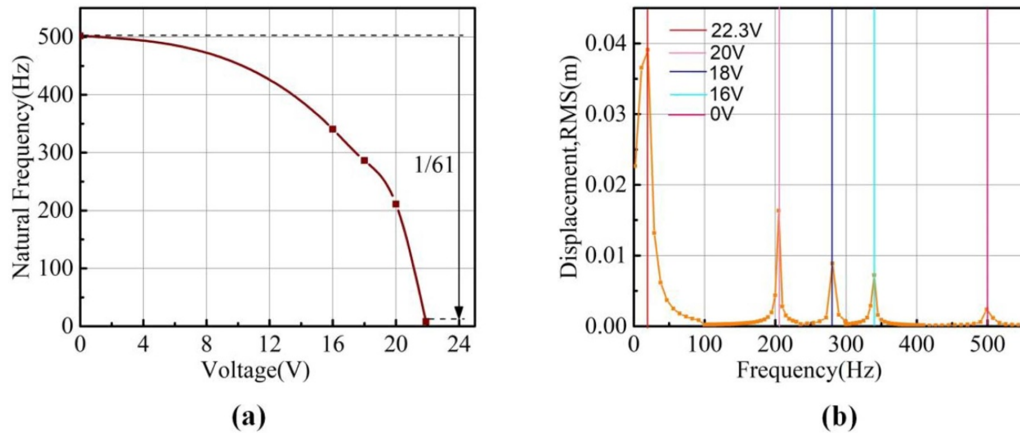

Figure 7. (a) Simulated frequency of the first mode versus applied voltage. (b) Simulated frequency response analysis.

voltage to realize quasi-zero stiffness, and simultaneously having a possibility to reach the allowable stress like the situation of $\gamma = 55$. Thus, we can choose a larger γ to make the springs-mass system has the quasi-zero stiffness characteristic at a low stress compressed state like the area I and II (the colored area). However, if γ is too large, it causes a difficulty in fabrication and the decline of structural rigidity. Therefore, a more appropriate parameter space for beam dimension is located in area I that is between the curves of around $\gamma = 60$ and $\gamma = 90$. In this work, a beam length-width ration of 90 was chosen. Finally, noting that the left y-axis is scaled by P/P_{cr} at $L_0 = 2$ mm and $\gamma = 90$, it is obvious that the critical value for the buckling is far from the brown area I.

3. Multiphysical simulation and discussion

In this section, a multiphysical model of microgravity accelerometer including Electric, Solid Mechanics and Heat Transfer modules is built up and simulated, in which the static structure and modal analysis are completed. As shown in figure 5(b), the simplified model was established in COMSOL Multiphysics 5.1a. To reduce the computation cost, the original frame component is omitted for achieving high quality mesh and convergence of the solution. The triangular elements are generated with totally 53 818 units, where the minimum size is 1.57×10^{-2} mm. Figure 5(b) also shows the external variable loads, such as the loading force and the applied voltage (up and down symmetrically), as well as the internal conditions including the choice of fixed boundaries (left and right symmetrically) and different region where the two kinds of heat transfer are used. Relevant parameters used in the modelling are listed in table 1. The simulation results are analyzed in details in the next section.

3.1. Modal and harmonic analysis

Firstly, we obtain the resonant frequencies by FE analysis when there is no DC voltage applied. As shown in figure 6, the first three modes of the microgravity accelerometer are respectively the in-plane mode (501.95 Hz), out-of-plane mode (712.26 Hz) and twisting mode (981.17 Hz).

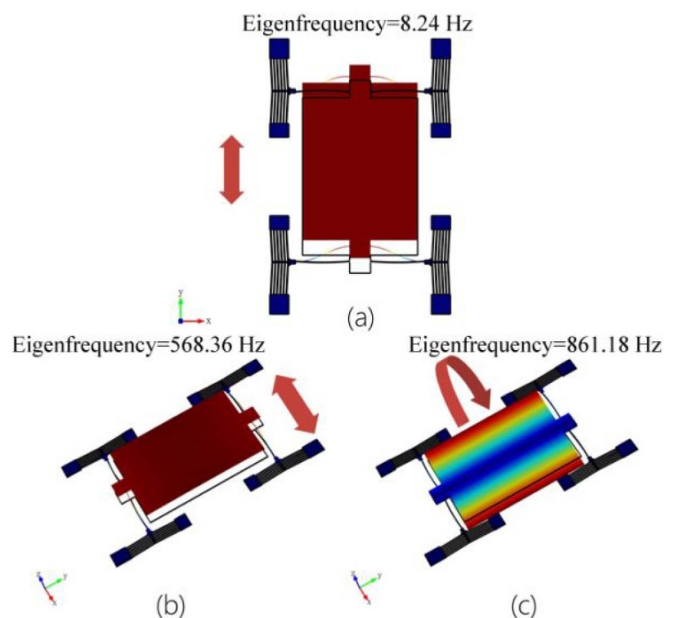

Figure 8. Eigenmodes of the designed accelerometer with an applied voltage of 22.3 V from COMSOL: (a) in-plane up and down mode; (b) out-of-plane mode; (c) twisting mode.

The relationship between the frequency of first-order mode of the accelerometer and the applied voltage was studied. The corresponding eigenfrequencies are obtained and plotted in figure 7(a) for different voltages in the interval of 0 V $\sim$ 22.3 V. It can be seen from figure 7(a) that the eigenfrequency decreases with the increased voltage, indicating that loading mechanism is effective and the resonant frequency can be adjusted by changing the applied voltage, which is due to the tuning of spring stiffness through the axial output displacement of the electrothermal actuators. Subsequently, a vertical harmonic excitation load was introduced to the proof mass in COMSOL using the prestressed frequency analysis module, the frequency response results at different voltages are shown in figure 7(b). It can be seen that in the frequency range of 0

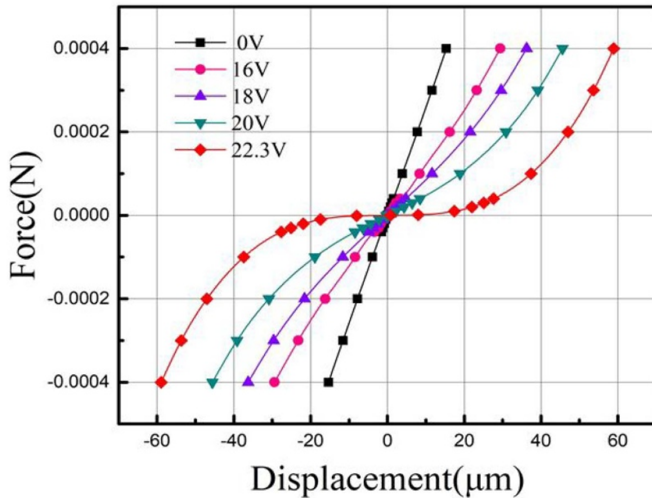

Figure 9. Simulated force-displacement curves (in y-axis direction) of the accelerometer.

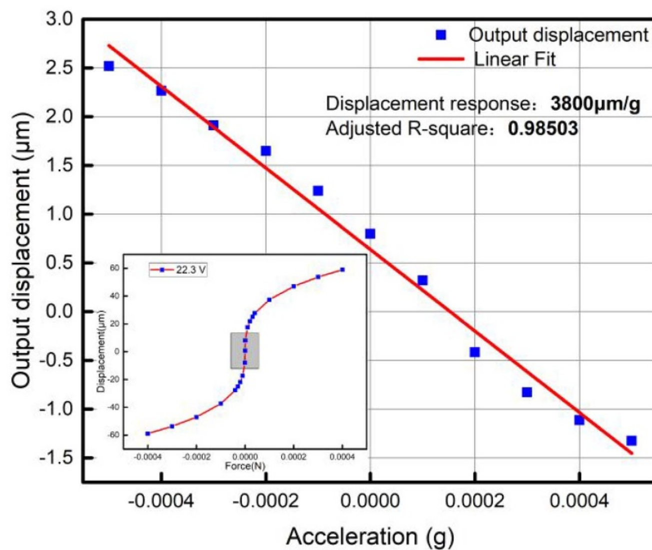

Figure 10. Acceleration—displacement output curve of microgravity accelerometer at 22.3 V loading voltage.

to 530 Hz, the five peaks corresponds well to the first-order mode frequency obtained in the modal analysis.

At the voltage of 22.3 V applied on the electrothermal actuators, one can be seen from figure 8 that the first-order frequency of the microgravity accelerometer is greatly reduced to about 8.24 Hz, while the second and third order modes are only slightly influenced, far from the first-order frequency. It is well-known that an ideal system should have a low frequency in one sensitive axis, and relatively high frequencies for other higher modes, which means that there will be little modal interaction of the device. This design achieves a ratio of 1:70 between the first and second modes, effectively depressing cross-sensitivity and making the measurement of its displacement much simpler.

Table 2. Comparison of performances of some of the reported microgravity accelerometers with our designed devices.

Reference	Simulated resonant frequency (Hz)	Calculated mechanical sensitivity (μm g^{-1})	Spring's length (mm)
[41]	2.3	46 925	nearly 6.5
[36]	3.1	25 831	nearly 8
[30]	1.68	87 952	nearly 3.6
This work	8.24	3800	nearly 2.16

3.2. Static performance analysis

The natural frequency of a mass spring system is given by $f_n = \frac{1}{2\pi}\sqrt{\frac{k}{m}}$, which depends only on its mechanical stiffness k when the proof mass m is determined. In addition, as discussed in section 2, it is better that the mechanical stiffness is lower in the working range but is larger beyond the working range to protect the structure be destroyed in case of overloading like a shock. Therefore, starting from the static equilibrium position of the proof mass, the force-displacement relationship of the proof mass is studied by applying an external force on it while the micro electrothermal actuator is driven by different voltages. As shown in figure 9, it is clear that the force-displacement relationship is gradually modulated from linear to nonlinear after increasing the voltage and a quasi-zero stiffness effect appears near the equilibrium position when the voltage is 22.3 V, which indicates that the mechanical stiffness of the designed microgravity accelerometer can be adjusted to meet the requirement from desired performance. As expected, when the proof mass is subjected to an overloading like a sudden larger acceleration, the nonlinear mechanical stiffness will prevent the accelerometer from a large displacement.

Another interesting point is the bandwidth of the quasi-zero stiffness region, in which the input acceleration and output displacement is expected to be a linear relationship. As shown in figure 10, the blue point is the output displacement and the solid red line is the fitting result, using the data from inset force-displacement curve at 22.3 V. The line shows a good fit, giving a scale factor of 3800 μm g^{-1} (that is equivalent to a vertical stiffness of 0.007N m^{-1}) within a range of $\pm$400 μg.

A comparison of the microgravity accelerometers' performance between reported and our design is given in table 2 in terms of resonant frequency, mechanical sensitivity and spring's length. Our design provides a controllable mechanical sensitivity and a tunable measurement range depending on the loading effect of electrothermal actuator. Furthermore, the spring's length is relatively shorter and a good anti-cross interference is obtained.

3.3. Thermal and stress analysis

Finally, the microgravity accelerometer structure was analysed in terms of safety. The overall simulated temperature field of the model is discussed at the maximum voltage 22.3 V, which accordingly causes highest temperature of the structure.

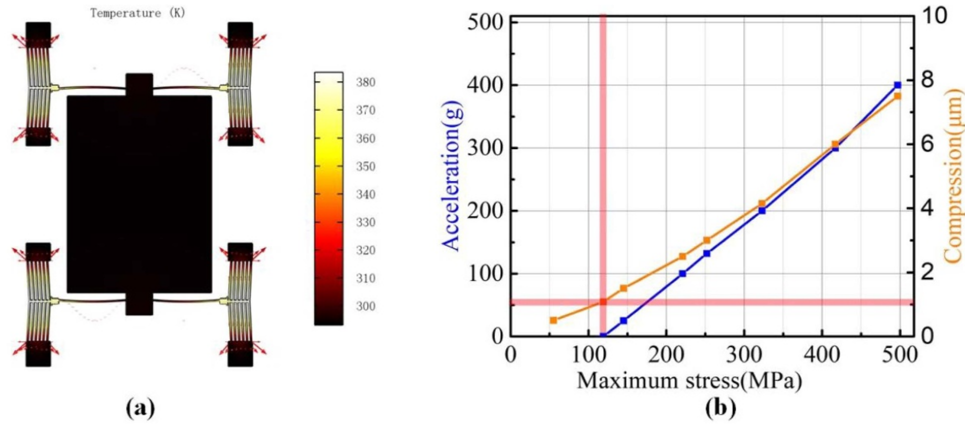

Figure 11. (a) Simulated temperature field at an applied voltage of 22.3 V.(b) Impact resistance simulation analysis.

The eight electrode anchors are integrated with the frame, so the anchor temperature is set to an ambient temperature of 293 K. The heat generated by the current can be transferred through the whole model. It can be seen from figure 11(a) that the maximum temperature of 380 K (about 107 °C) occurs at the centre of the electrothermal actuator where the curved beam is connected. Since the potential is symmetric under ideal conditions, the proof mass does not pass any current and the temperature does not change substantially. For silicon substrate, creep and plastic deformation usually do not occur below 800 °C, so the temperature rise at 22.3 V is safe for the device.

Moreover, the impact resistance of the microgravity accelerometer was analysed. The previous discussion indicates when the device works beyond the quasi-zero stiffness region, its stiffness begins to rise, so we apply a large vertical load directly to the structure to check its maximum stress. As shown in figure 11(b), the maximum stress of the structure exceeds the allowable stress of 500 MPa when the imposed acceleration exceeds 400 g, which will equivalently induce a compression displacement of nearly 8 μm. The crossover point represents the stress around 1.08 μm compression displacement, which equals the stress value resulted from the micro electrothermal actuator at an applied voltage of 22.3 V. It is clear that is sufficiently safe for the microgravity accelerometer application.

3.4. Effect of manufacturing uncertainty

In the microfabrication process, manufacturing errors are indeed unavoidable. For example, the align errors in photolithography process and the under etching in pattern transfer process are typical manufacturing errors. Hence, the dimensions of fabricated micro devices will not be the same as designed and variations of feature size are normally of microns or less depending on the manufacturing capability. In this design, the length of key structures is in mm scale, but their width are mostly in micro scale and therefore the effect of manufacturing errors on the line width of curved beams and actuator beams are considered.

Obviously, the line width error directly change the stiffness and mass and accordingly change the system resonant frequency. Based on the analysis in section 2, the axis stiffness K are controlled by β and λ. The K_v in figure 1(b) can be expressed by $K_v = 12EI/{L_0}^3$, in which the curved beams' moment of inertia is $I = tw^3/12$. The K_h in equation (13) can also be written by using I, namely proportional to w^3. Therefore, if a width error added to original w, the applied voltage would change due to the affected K_h, which can be seen from figure 5(a) that the three black rhombus marks with different width of curved beam share the same location at horizontal axis. To evaluate the effect of manufacturing error, the FEA model in figure 5(b) was employed to study the changes of resonant frequency and applied voltage subject to dimensional change. In the simulation, the line width was adjusted within ±9% as compared with its design value. As shown in table 3, the resonant frequency of device changes slightly. The line width error mainly affects the applied voltage when the system reaches the quasi-zero stiffness. However, the changes of resonant frequeny and applied voltage are still acceptable. Once the manufacturing errors are known in the pratical experiments, their effects can be compensated by modifying the geometrical design according to the desired performance.

Table 3. The impact of manufacturing parameter uncertaintiy on device's characterustic.

Line width error	−9%	−4.5%	0%	4.5%	9%
Simulated resonant frequency (Hz)	10.4	8.47	8.24	8.15	8.07
Applied voltage (V)	19.2	21.4	22.3	23.2	24

4. Conclusion

In this paper, we present a design, modelling and simulation of an accelerometer with quasi-zero-stiffness, which could be utilized for the microgravity measurement. The concept of anti-spring structure is adopted in the design. Particularly, micro electrothermal actuators are used to tune the axial stress of the spring structure, leading to a quasi-zero-stiffness behavior of the designed microgravity accelerometer. When the electrothermal actuator is driven at 22.3 V, the

natural frequency is decreased from 501.95 Hz to 8.24 Hz while the other two nearby modes are not much affected with their frequency remain above 500 Hz. The analysis of quasi-zero-stiffness region at 22.3 V leads to a scale factor of 3800 μm g^{-1} within a measurement range of $\pm$400 μg. Based on the electrothermal loading mechanism, one can adjust stiffness and frequency of accelerometer according to the measurement demands. Additionally, the designed microgravity accelerometer has a large impact resistance and it is safe to use at the applied voltage. It is expected that the proposed device can be used in microgravity acceleration measurement and related applications.

Acknowledgments

This work is financially supported by the National Key R & D Program of China (2018YFB2002303), Key research and development program of Shaanxi Province (2018ZDCXL-GY-02-03), National Natural Science Foundation of China (51575439) and 111 project (B12016). We also appreciate the support from State Key Laboratory of applied optics and International Joint Laboratory for Micro/Nano Manufacturing and Measurement Technologies.

ORCID iD

Xueyong Wei https://orcid.org/0000-0002-6443-4727

References

[1] Laine J and Mougenot D 2014 A high-sensitivity mems-based accelerometer *Lead. Edge* **33** 1234–42
[2] Jiang Z *et al* 2012 Relative gravity measurement campaign during the 8th international comparison of absolute gravimeters (2009) *Metrologia* **49** 95–107
[3] Krishnamoorthy U *et al* 2008 In-plane MEMS-based nano-g accelerometer with sub-wavelength optical resonant sensor *Sensors Actuators* A **145–6** 283–90
[4] Wu W *et al* 2016 Novel capacitive sensing system design of a microelectromechanical systems accelerometer for gravity measurement applications *Micromachines* **7** 167
[5] Pike W T *et al* 2018 A broad-band silicon microseismometer with 0.25 ng/rtHz performance *IEEE 31st Micro Electro Mechanical Systems (MEMS 2018) (Belfast)* pp 113–16
[6] Kavitha S, Daniel R J and Sumangala K 2013 A simple analytical design approach based on computer aided analysis of bulk micromachined piezoresistive MEMS accelerometer for concrete SHM applications *Measurement* **46** 3372–88
[7] Plaza J *et al* 2004 BESOI-based integrated optical silicon accelerometer *J. Microelectromech. Syst.* **13** 355–64
[8] Teo A J T *et al* 2017 An optical MEMS accelerometer fabricated using double-sided deep reactive ion etching on silicon-on-insulator wafer *J. Micromech. Microeng.* **27** 067001
[9] Teo A *et al* 2016 Highly sensitive optical motion detector *Symp. on Design, Test, Integration & Packaging of Mems/Moems* (IEEE)
[10] Teo A *et al* 2017 Design optimization for an SOI MOEMS accelerometer *Microsyst. Technol.*
[11] Hortschitz W *et al* 2011 An optical in-plane MEMS vibration sensor *IEEE Sens. J.* **11** 2805–12
[12] Hortschitz W *et al* 2014 MOEMS vibration sensor for advanced low-frequency applications with pm resolution *Procedia Eng.* **87** 835–8
[13] Kainz A *et al* 2018 Distortion-free measurement of electric field strength with a MEMS sensor *Nat. Electron.* **1** 68–73
[14] 2012 Robust precision position detection with an optical MEMS hybrid device *IEEE Trans. Ind. Electron.* **59** 4855–62
[15] Hortschitz W *et al* 2014 Novel high resolution MOEMS inclination sensor *2014 IEEE Sensors* (*IEEE*)
[16] Hammer G *et al* 2018 Detection of heart and respiration rate with an organic-semiconductor-based optomechanical MEMS sensor *Proc. (American Bar Association. Section of Int. and Comparative Law)* vol 2
[17] Nguyen D S *et al* 2010 Fabrication and characterization of a wideband MEMS energy harvester utilizing nonlinear springs *J. Micromech. Microeng.* **20** 125009
[18] Nguyen C H *et al* 2014 Experimental validation of damping model for a MEMS bistable electrostatic energy harvester *J. Phys.: Conf. Ser.* **557** 012114
[19] Vysotskyi B *et al* 2016 Innovative energy harvester design using bistable mechanism with compensational springs in gravity field *J. Phys. Conf. Ser.* **773** 012064
[20] Vysotskyi B *et al* 2017 Engineering the structural nonlinearity using multimodal-shaped springs in MEMS *J. Microelectromech. Syst.* **27** 40–6
[21] Vysotskyi B *et al* 2018 Nonlinear electrostatic energy harvester using compensational springs in gravity Field *J. Micromech. Microeng.* **28** 074004
[22] Yamamoto K *et al* 2015 Design and abrication of parallel curved spring for nonlinear energy harvester *Procedia Eng.* **120** 651–4
[23] Yamamoto K *et al* 2015 Vibration energy harvester with bi-stable curved beam spring offset by gravitational acceleration *J. Phys.: Conf. Ser.* **660** 012127
[24] Yamamoto K *et al* 2014 A design of mechanical frequency converter linear and non-linear spring combination for energy harvesting **557** 012065
[25] Shmulevich S, Hotzen I and Elata D 2013 A perfect electrostatic anti-spring *Proc. SENSORS 2013* pp 1–4
[26] Tvedt L G W, Nguyen D S and Halvorsen E 2010 Nonlinear behavior of an electrostatic energy harvester under wide- and narrowband excitation *J. Microelectromech. Syst.* **19** 305–16
[27] Bramsiepe S G *et al* 2018 A high stability optical shadow sensor with applications for precision accelerometers *IEEE Sens. J.* **18** 4108–16
[28] Thorby D 2013 *Structural Dynamics and Vibration in Practice* (London: Butterworth-Heinemann)
[29] Middlemiss R P *et al* 2016 Measurement of the Earth tides with a MEMS gravimeter *Nature* **531** 614–17
[30] Mansouri B E, Middelburg L M, Poelma R H *et al* 2019 High-resolution MEMS inertial sensor combining large-displacement buckling behaviour with integrated capacitive readout *Microsyst. Nanoeng.* **5** 60
[31] Zhanga H, Weia X, Ding Y *et al* 2019 A low noise capacitive MEMS accelerometer with anti-springstructure *Sensors Actuators* A **296** 79–86
[32] Anvar V, Alexey Z and Artem T 2017 Study of application of vibration isolators with quasi-zero stiffness for reducing dynamics loads on the foundation *Procedia Eng.* **176** 137–43
[33] Lan C C, Yang S A and Wu Y S 2014 Design and experiment of a compact quasi-zero-stiffness isolator capable of a wide range of loads *J. Sound Vib.* **333** 4843–58

[34] Thanh Danh L E and Ahn K K 2010 The static characteristic of a vibration isolating system with a low dynamic stiffness characteristic *Int. Conf. on Control Automation & Systems* (*IEEE*)
[35] Ishida S, Suzuki K and Shimosaka H 2017 Design and experimental analysis of origami-inspired vibration isolator with quasi-zero-stiffness characteristic *J. Vib. Acoust.* **139** 051004
[36] Tang S, Liu H, Yan S *et al* 2019 A high-sensitivity MEMS gravimeter with a large dynamic range *Microsyst. Nanoeng.* **5** 45
[37] Kavitha S, Joseph Daniel R and Sumangala K 2016 High performance MEMS accelerometers for concrete SHM applications and comparison with COTS accelerometers *Mech. Syst. Signal Process.* **66–67** 410–24
[38] Carrella A, Brennan M J, Waters T P *et al* 2012 Force and displacement transmissibility of a nonlinear isolator with high-static-low-dynamic-stiffness *Int. J. Mech. Sci.* **55** 22–29
[39] Gianchandani Y B and Najafi K 1996 Bent-beam strain sensors *J. Microelectromech. Syst.* **5** 52–58
[40] Virgin L N and Davis R B 2003 Vibration isolation using buckled struts *J. Sound Vib.* **260** 965–73
[41] Middlemiss R P 2016 A practical MEMS gravimeter *PhD Thesis* (University of Glasgow)